Supplement of Nat. Hazards Earth Syst. Sci., 26, 5791–5813, 2026
https://doi.org/10.5194/nhess-26-5791-2026-supplement
© Author(s) 2026. CC BY 4.0 License.



Natural Hazards and Earth System Sciences
Open Access
EGU

Supplement of

Scaling and exceedance probability of sinkhole collapse in evaporite karst (Dead Sea, Jordan)

Hanna Z. Schulten et al.

Correspondence to: Eoghan P. Holohan (eoghan.holohan@ucd.ie)

The copyright of individual parts of the supplement might differ from the article licence.

Section S1: Satellite and aerial imagery metadata and pre-processing information

Table S1: Metadata for high resolution satellite and aerial imagery used for mapping sinkholes on the Dead Sea's eastern shore. (RJGC = Royal Jordanian Geographical Centre). The ground sample distance is the side length of one image pixel as it relates to the land/lake surface.

Year	Sensor/Source	Date Acquired	Acquisition Time (UTC)	Off-Nadir View Angle (°)	Collection Azimuth	Ground sample distance (m)
1967	Corona (USGS)	n/a	n/a	n/a	n/a	2.0
1992	Airborne Camera (RJGC)	n/a	n/a	n/a	n/a	0.6
2000	Airborne Camera (RJGC)	n/a	n/a	n/a	n/a	0.6
2002	Quickbird	2002-06-19	08:14	25.4	62.6	0.61
2002	Quickbird	2002-07-07	08:14	25.1	106.3	0.61
2004	Quickbird	2004-10-20	08:21	12	90.1	0.61
2005	Quickbird	2005-10-28	08:37	3.3	120.1	0.61
2006	Quickbird	2006-11-18	08:42	11	131.3	0.61
2007	Quickbird	2007-08-28	08:43	13.8	161.9	0.61
2008	Worldview 1	2008-04-20	08:26	18.3	240.3	0.5
2009	GeoEye-1	2009-08-09	08:32	19.3	223.9	0.5
2010	GeoEye-1	2010-07-29	08:27	13.2	226.3	0.5
2011	Worldview 1	2011-08-26	08:38	5.2	104.7	0.5
2012	Quickbird	2012-03-05	07:42	19.8	119	0.61
2013	Pleiades-1A	2013-06-19	08:29	23.9	179.9	0.5
2014	Worldview 3	2014-09-23	08:06	21.1	59.8	0.3
2014	UAV-based camera (orthomosaic)	2014-10	Various	Various	Various	0.1
2015	Pleiades-1A	2015-06-05	08:21	21.8	180.1	0.5
2015	UAV-based camera (orthomosaic)	2015-10	Various	Various	Various	0.1
2016	Pleiades-1A	2016-04-25	08:20	20.6	180.1	0.5
2016	UAV-based camera (orthomosaic)	2016-11	Various	Various	Various	0.1
2017	Pleiades-1A	2017-04-16	08:31	7.1	180.1	0.5
2018	Pleiades-1B	2018-04-23	08:23	19.6	180.1	0.5
2019	Pleiades-1B	2019-07-28	08:25	14.3	180.1	0.5
2020	Pleiades-1A	2020-04-12	08:33	27.1	180.1	0.5
2021	Pleiades-Neo	2021-08-18	08:14	25.7	97.9	0.3
2021	Pleiades-1A	2021-10-23	08:33	22.7	180.1	0.5
2022	Pleiades-1A	2022-01-29	08:28	7.2	180.1	0.5
2022	Pleiades-1B	2022-04-25	08:17	27.7	180.1	0.5
2022	Pleiades-Neo	2022-08-02	08:29	19.6	97.9	0.3
2023	Pleiades-1B	2023-11-08	08:29	15.3	128.9	0.5
2024	Pleiades-Neo	2024-01-22	12:18	28.1	97.9	0.3

Table S2: Pre-processing of satellite imagery, including information regarding software used for orthorectification and pansharpening, the Digital Elevation Model (DEM) used as the elevation reference for the orthorectification, and any additional operations made using GDAL/OGR. The DEMs listed here are coarse-resolution (~30m) global elevation datasets used only as input to orthorectification. They are distinct from high-resolution (0.1m) digital surface models (DSMs) generated from the photogrammetric surveys.

Year	Orthorectification and Pansharpening Software	DEM used in Orthorectification	Additional Georeferencing using GDAL/OGR?
1992	Aerial photography	n/a	n/a
2000	Aerial photography	n/a	n/a
2002	PCI	SRTM	Yes
2002	PCI	SRTM	Yes
2004	PCI	SRTM	Yes
2005	PCI	SRTM	Yes
2006	PCI	SRTM	Yes
2007	ERDAS	n/a	No
2008	ERDAS	n/a	No
2009	ERDAS	n/a	No
2010	ERDAS	n/a	No
2011	ERDAS	n/a	No
2012	PCI	ASTER	Yes
2012	ERDAS	n/a	No
2013	ERDAS	n/a	Yes
2014	PCI	JAXA	Yes
2015	ERDAS	n/a	Yes
2016	PCI	Elevation 30 (Airbus)	No
2017	PCI	Elevation 30 (Airbus)	No
2018	PCI	Elevation 30 (Airbus)	No
2019	ArcGIS pro	Elevation 30 (Airbus)	No
2020	ArcGIS pro	Elevation 30 (Airbus)	No
2021	ArcGIS pro	Elevation 30 (Airbus)	No
2021	ArcGIS pro	Elevation 30 (Airbus)	No
2022	ArcGIS pro	Elevation 30 (Airbus)	No
2022	ArcGIS pro	Elevation 30 (Airbus)	No
2022	ArcGIS pro	Elevation 30 (Airbus)	No
2023	n/a	n/a	No
2024	n/a	n/a	No

Section S2: Analysis of field-based sinkhole inventory for years prior to 2000

Prior to high-resolution satellite imagery being readily available for the Ghor Al-Haditha sinkhole area, researchers from the Jordanian Ministry for Energy and Mineral Resources created a sinkhole inventory based on fieldwork and communication with local farmers and landworkers (El-Isa et al., 1995; Sawarieh et al., 2000). After deriving an initial sinkhole inventory from the same aerial photograph from 1992 as we have used in this study, these authors produced a complimentary field-based record of the sinkhole time series for the period from 1985 to 1999. To supplement direct field observations, they also communicated with farmers about infilled and historic sinkholes, of which they recorded at least 22 instances. According to Table 1.1 of Sawarieh et al. (2000), 88 sinkholes were formed prior to 2000 (see **Table S3**). The presence of 23 of these is confirmed in the aerial photograph from 1992, with these being in the north-eastern arm of uvala U2 and in the alluvial fan just north of the Wadi Ibn Hamad.

The extent of the influence of sparse observations and infilling of sinkholes on our data is difficult to accurately quantify for a number of reasons. Firstly, Sawarieh et al. did not provide precise dates of formation for most of the sinkholes in their records. Their method of recording sinkhole instances was to split the southern part of the Ghor Al-Haditha sinkhole area (i.e. the alluvium deposits) into subsidence zones where clusters of sinkholes had formed. The clusters are labelled A - I and are geographically ordered north to south (cf. Fig 2.2, Sawarieh et al., 2000), with A being the most northerly and I the most southerly. Zones A - C are within uvala U2; D - F are dispersed parallel to the shoreline across the alluvial fan; G are in the area of uvala U1; H is within the bed of the Wadi Ibn Hamad; and I is just south of Wadi Ibn Hamad. They then assigned ranges for the year of formation to each cluster. In general, these date ranges for the clusters reflect the same northerly migration of sinkhole formation as observed across our full time series dataset for years until 2024. When we were interpreting these date ranges, we took the earliest possible date in the range offered (see **Table S3**), so as to examine the most significant possible deviation from our observed trend of accelerating sinkhole formation as time progressed. **Table S4** shows the cumulative evolution of the sinkhole count and area over time as per their sinkhole inventory.

Table S3: records of field observations of sinkhole formation prior to 2000, after Sawarieh et al. (2000). The 'Confidence in year' field is a qualitative assessment which we have made based on the information provided by Sawarieh et al. (e.g., whether a specific year was named in the notes, how wide the range of possible formation dates is, completeness of notes, etc). The areas are calculated by approximating the sinkholes as circles/ellipses, by using the formula $A = \pi xy$ where A is the area, x is the width and y is the length.

Hole ID	Year of formation	Earliest possible year of formation	Confidence in year	Length (m)	Width (m)	Area (m^2)
A-1	1995 - 1999	1995	Medium	8.2	4.9	126.23
A-2	1995 - 1999	1995	Medium	3.05	1.78	17.06
A-3	1995 - 1999	1995	Medium	0.47	0.5	0.74
A-4	1995 - 1999	1995	Medium	1.68	1.68	8.87
A-5	1995 - 1999	1995	Medium	2.1	2.1	13.85
A-6	1995 - 1999	1995	Medium	1.3	1.5	6.13
A-7	1995 - 1999	1995	Medium	4.92	4.92	76.05
A-8	1995 - 1999	1995	Medium	3.45	3	32.52
A-9	1995 - 1999	1995	Medium	23	17.5	1,264.49
A-10	1995 - 1999	1995	Medium	2.33	2.33	17.06
A-11	1995 - 1999	1995	Medium	3.1	3.1	30.19
A-12	1995 - 1999	1995	Medium	5.34	5.34	89.58

A-13	1995 - 1999	1995	Medium	2.54	2.54	20.27
A-14	1995 - 1999	1995	Medium	15.55	14.8	723.01
A-15	1995 - 1999	1995	Medium	2.84	2.84	25.34
A-16	1995 - 1999	1995	Medium	3.4	2.2	23.50
A-17	1995 - 1999	1995	Medium	5.7	5.7	102.07
A-18	1995 - 1999	1995	Medium	6.6	6.6	136.85
A-19	1995 - 1999	1995	Medium	2.4	2.4	18.10
A-20	1995 - 1999	1995	Medium	10.1	10	317.30
A-21	1995 - 1999	1995	Medium	26.4	26.4	2,189.56
A-22	1995 - 1999	1995	Medium	8.95	8.95	251.65
A-23	1995 - 1999	1995	Medium	10.6	10.6	352.99
A-24	1995 - 1999	1995	Medium	7.4	7.4	172.03
A-25	1995 - 1999	1995	Medium	4.9	4.9	75.43
A-26	1995 - 1999	1995	Medium	12.8	12.8	514.72
A-27	1995 - 1999	1995	Medium	4.1	4.1	52.81
A-28	1995 - 1999	1995	Medium	7.1	7.1	158.37
A-29	1995 - 1999	1995	Medium	5.4	5.4	91.61
A-30	1995 - 1999	1995	Medium	6.3	6.3	124.69
A-31	1995 - 1999	1995	Medium	3.75	3.75	44.18
A-32	1995 - 1999	1995	Medium	10.3	10.3	333.29
A-33	1995 - 1999	1995	Medium	3.5	3.5	38.48
A-34	1995 - 1999	1995	Medium	5.85	5.85	107.51
A-35	1995 - 1999	1995	Medium	6.7	6.7	141.03
A-36	1995 - 1999	1995	Medium	5.1	5.1	81.71
A-37	1995 - 1999	1995	Medium	3.6	3.6	40.72
A-38	1995 - 1999	1995	Medium	2.6	2.6	21.24
A-39	1995 - 1999	1995	Medium	49	40	6,157.52
A-40	1995 - 1999	1995	Medium	4.4	4.4	60.82
B-1	1997 - 1999	1997	Medium	8.6	8.6	232.35
B-2	1997 - 1999	1997	Medium	2.5	2.5	19.63
B-3	1997 - 1999	1997	Medium	1.6	1.6	8.04
B-4	1997 - 1999	1997	Medium	5.1	5.1	81.71
B-5	1997 - 1999	1997	Medium	3	3	28.27
B-6	1997 - 1999	1997	Medium	5.1	5.1	81.71
B-7	1997 - 1999	1997	Medium	9.7	9.7	295.59
B-8	1997 - 1999	1997	Medium	4.6	4.6	66.48

B-9	1997 - 1999	1997	Medium	4.1	4.1	52.81
B-10	1997 - 1999	1997	Medium	5.1	5.1	81.71
B-11	1997 - 1999	1997	Medium	4.6	4.6	66.48
B-12	1997 - 1999	1997	Medium	25	25	1,963.50
B-13	1997 - 1999	1997	Medium	2.6	2.2	17.97
C-1	1985 - 1999	1985	Low	0.6	0.55	1.04
C-2	1998	1998	High	32	30	3,015.93
C-3	1994	1994	High			0.00
C-4	1985 - 1999	1985	Low			0.00
C-5	1985 - 1999	1985	Low			0.00
C-6	1985 - 1999	1985	Low			0.00
C-7	1985 - 1999	1985	Low			0.00
D-1	1995	1995	High	25	23.5	1,845.69
D-2	1998	1998	High	17.5	15	824.67
E-1	1997	1997	High	5	5	78.54
E-2	1998	1998	High	4	4	50.27
E-3	1999	1999	High	4.6	4.6	66.48
E-4	1969 - 1999	1969	Low	10	10	314.16
E-5	1969 - 1999	1969	Low	4.3	4.2	56.74
E-6	1969 - 1999	1969	Low	4.4	4.4	60.82
E-7	1969	1969	Medium	2	2	12.57
F-1	1994 - 1999	1994	Low	18	18	1,017.88
F-2	1997	1997	High	20	20	1,256.64
F-3	1998	1998	High	2	2	12.57
F-4	1998	1998	High	1.5	1.5	7.07
F-5	1985	1985	High			0.00
G-1	1992	1992	High	24.5	19.5	1,500.90
G-2	1986 - 1992	1986	Low	5.2	4.2	68.61
G-3	1986 - 1992	1986	Low	4.7	2.9	42.82
G-4	1992	1992	High	34	33	3,524.87
H-1	1985	1985	High	12.8	11.5	462.44
H-2	1985 - 1999	1985	Low	10.4	6	196.04
H-3	1985 - 1999	1985	Low	3.4	3.4	36.32
H-4	1985 - 1999	1985	Low	5	4.6	72.26
I-1	1985	1985	High	5.5	5.3	91.58
I-2	1985 - 1999	1985	Low	5.2	3.5	57.18

I-3	1985 - 1999	1985	Low	5.7	5.7	102.07
I-4	1985 - 1999	1985	Low	47	40	5,906.19
I-5	1999	1999	High	1.8	2.5	14.14
I-6	1999	1999	High	24.5	24.5	1,885.74

Table S4: sinkhole count and estimated area for the period prior to 2000, as derived from Table S3. Counts for each year may be higher or lower than the true value, as the 'year' column represents the earliest possible year of formation based on the range of years (cf. Table S3).

Year	Count	Cumulative count	Area (m^2)	Cumulative area (m^2)
1969 - 1985	18	18	7,369.39	7,369.39
1986	2	20	111.43	7,480.82
1992	2	22	5,025.76	12,506.59
1994	2	24	1,017.88	13,524.46
1995	41	65	15,905.23	29,429.69
1997	15	80	4,331.44	33,761.13
1998	5	85	3,910.50	37,671.63
1999	3	88	1,966.35	39,637.98

An alternative cause of the non-linear increase in sinkhole count from 1992-2004 is that we have undercounted sinkholes in this time period because evidence of their formation was erased. Such undercounting is also unlikely to explain the non-linear trend prior to 2004, however, for two reasons. Firstly, if we assume that the post-2004 linear growth rate of ~100 new holes per year was in fact present from 1992-2004, then we would expect a population size of over 1300 holes by 2004. This would require the erasure or mismapping of about 1200 holes. However, independent mapping of the Ghor Al-Haditha sinkholes from the late 1980s through the 1990s from aerial photos and fieldwork, as compiled in the report by Sawarieh et al., (2000), gives cumulative counts of 22 sinkholes by 1992 and 88 sinkholes by 1999. This includes several sinkholes that were infilled by local farmers. Our independent mapping via remote sensing data yields 18 sinkholes formed by 1992 and 58 sinkholes formed by 2000, which indicates some infilling-related undercounting in this period, but perhaps only on the order of a few 10's of holes rather than > 1000 holes. Secondly, as noted above, the same non-linear trend from 1980s to mid-2000s is seen on the western shore, including in areas of no agricultural development (e.g. the Ze'elim alluvial fan) where there is no incentive for erasure or infilling of sinkholes. Thus, undercounting through erasure is also insufficient to cause the non-linearity of cumulative sinkhole count with time in Figure 7.

We performed the same size-frequency analysis on the data in Table S3 as we applied to our sinkhole data collected for years 2004 - 2024 (**Figs S1 and S2**). A comparison of the resulting distributions shows that the size-frequency distribution of holes as recorded by Sawarieh et al. are also better fit by a lognormal distribution than a powerlaw distribution. Although a powerlaw distribution provides a less poor fit to these earlier data, and fits equally well to a lognormal distribution over a wider range of lengths (xmin = 3.75 m) and areas (xmin = 42.8 m2), a lognormal distribution nevertheless fits the entire size distribution much better for both length and area domains (R = -47 in both cases; **Fig. S2**).

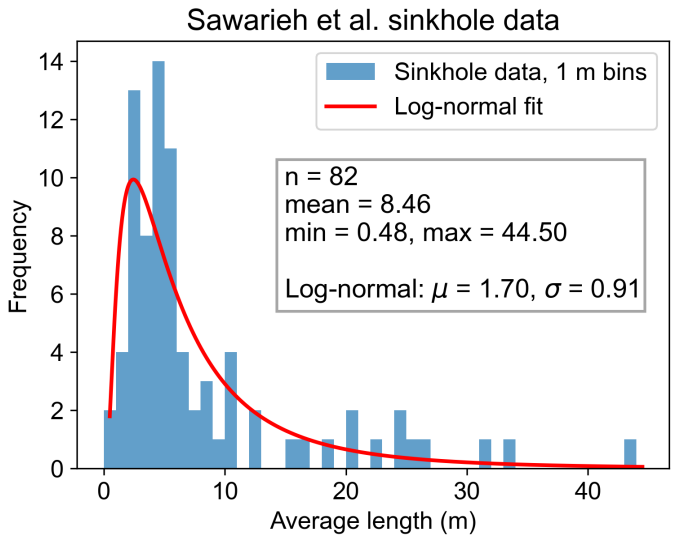


Figure S1: Sinkhole frequency distribution for sinkholes formed prior to 2000 as derived from (Sawarieh et al., 2000). The data are reasonably represented by a lognormal distribution. 6 sinkhole records do not have any length or width information (cf. **Table S3**), hence n is lower than in Table S3.

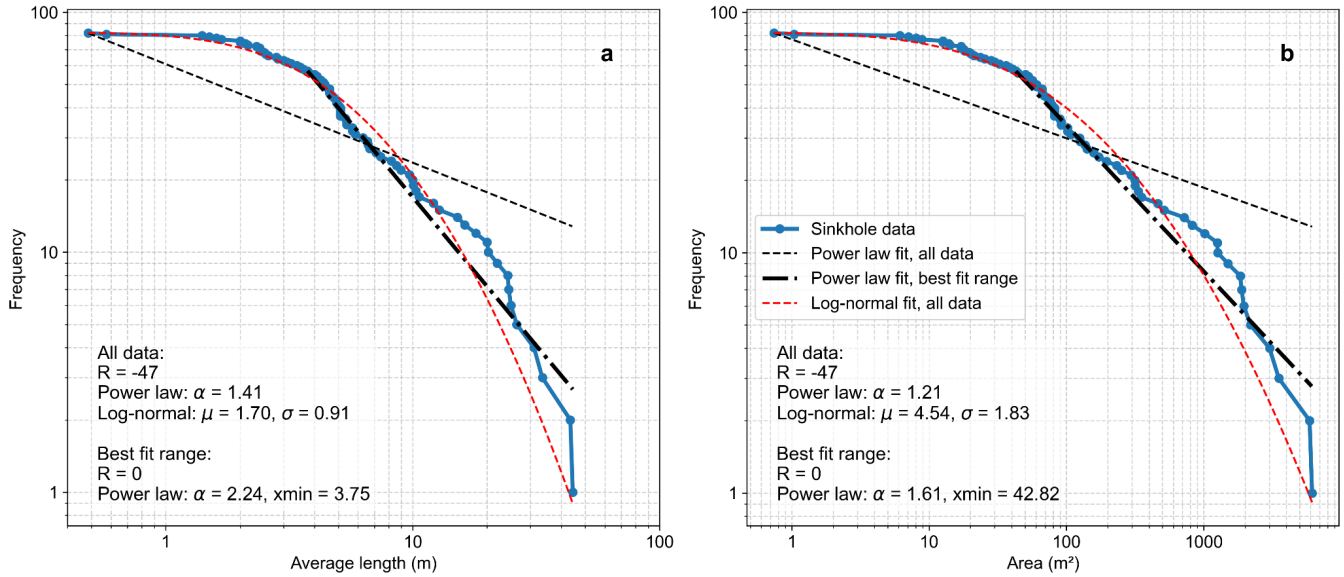


Figure S2: Cumulative frequency curves for (a) sinkhole average length and (b) sinkhole area for sinkholes formed prior to 2000 as derived from (Sawarieh et al., 2000).

Section S3: Influence of image resolution and operator variability on sinkhole mapping reproducibility

We have done an initial investigation into the impact of image resolution (Ground Sampling Distance, GSD) and operator variability into the count and area of mapped sinkholes. The mapping comparison was performed across three subset areas (**Fig. S3**), representing each of the dominant sinkhole-hosting materials (alluvium/south, mud/middle and salt/northern) for images acquired in 2021 and 2022; the original PNEO images with GSD 0.3 m pix-1 were downsampled for this analysis, to GSDs of 0.6 and 2 m pix-1. For each subset year and zone, the total point count of sinkholes was compared, alongside the count of sinkhole polygons and total area of sinkholes mapped. A single sinkhole polygon may represent multiple sinkhole instances when represented as points; as such, the number of sinkhole polygons mapped by each operator for a given zone and image resolution is generally lower than the number of points.

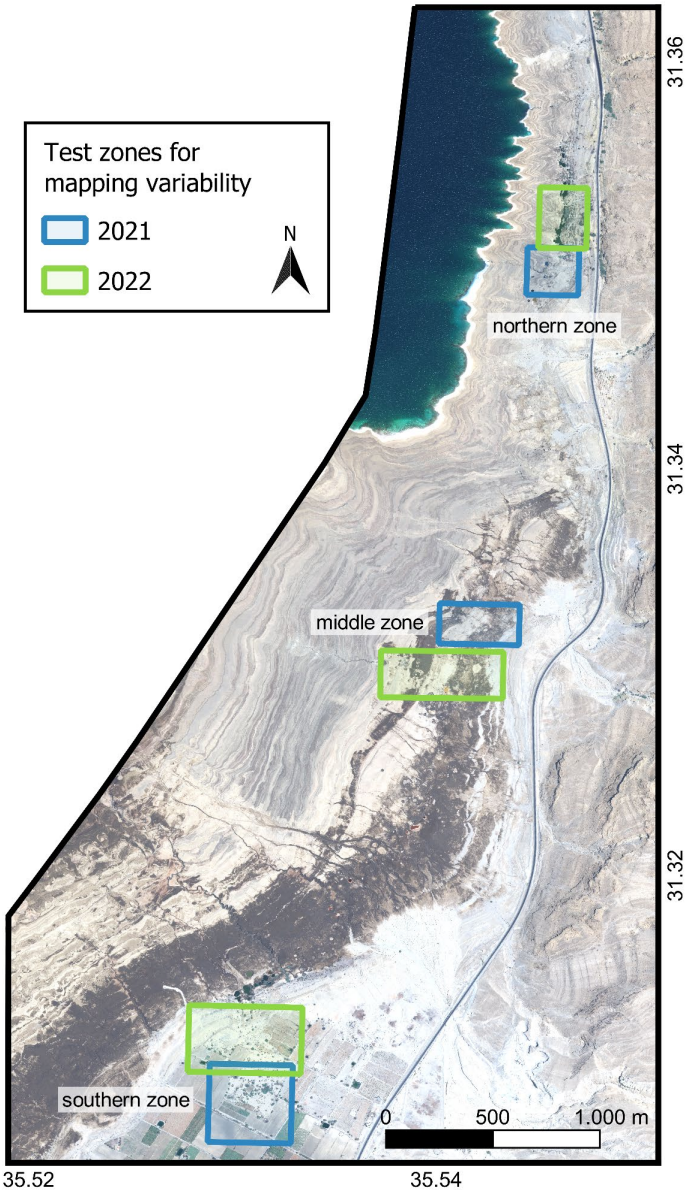


Figure S3: Map showing the six testing zones for comparing image resolution and operator impact and Hausdorff distance calculations. Blue zones are based on the 2021 Pléiades Neo satellite image (© Airbus DS 2021), and green zones on the 2022 Pléiades Neo satellite image (© Airbus DS 2022).

This test showed that image resolution exerts a strong control on detection. The number of sinkhole points mapped by each operator declined monotonically with coarsening GSD in every zone and year tested. Operators recovered a median of 80% of the 0.3 m pix^{-1} count at 0.6 m pix^{-1} and only 45% at 2 m pix^{-1} (Fig. S4). This loss falls almost entirely on the smallest sinkholes: features under 50 m² make up 36% of polygons mapped at 0.3 m pix^{-1} but fewer than 5% of those mapped at 2 m pix^{-1}, consistent with a detection threshold of 4 x 4 pixels. The equivalent trend in polygon count is weaker (Fig. S5), reflecting

the additional subjectivity in subdividing compound sinkholes. Total mapped area shows no such trend, and in several cases increases as imagery is coarsened (Fig. S6). This is because two effects act in opposition: small sinkholes are missed entirely, while those that remain visible are delineated more generously as edges are generalised and neighbouring depressions merge into single outlines. Median polygon area accordingly rises from 105 m² at 0.3 m pix^{-1} to 276 m² at 2 m pix^{-1}. The two operators differed by an average of 11% in point count but 16% in total mapped area. Sinkhole counts are therefore governed principally by image resolution and are comparatively reproducible between operators, whereas mapped area is influenced as much by operator delineation as by resolution. Because our scaling and exceedance probability analyses rest on counts and size distributions from the 2004–2024 period, for which imagery of consistently high resolution (0.6 - 0.1 m) is available, we consider the effect of these uncertainties on our principal results to be limited.

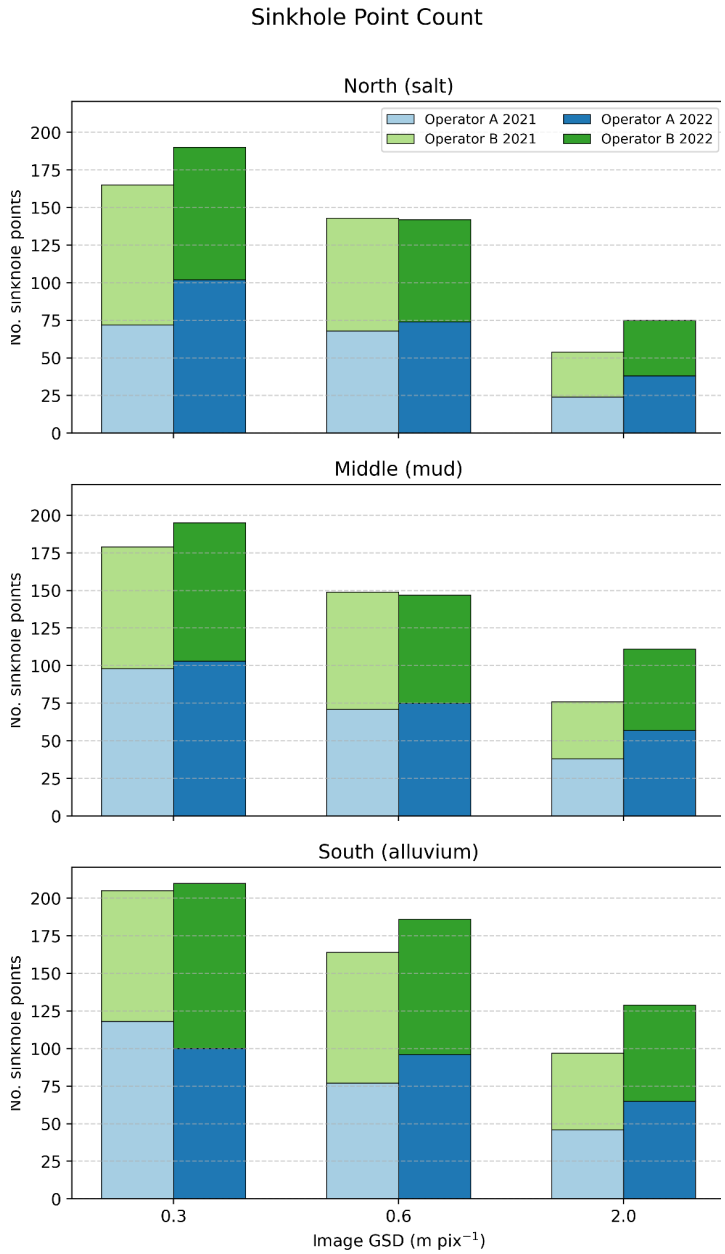


Figure S4: Sinkhole point count by operator for the three sample areas for the 2021 and 2022 satellite images. The sinkhole point counts are further classified based on GSD (0.3m pix-1, 0.6m pix-1, and 2m pix-1). The values in the table represent the number of sinkholes observed at each specified GSD within the given geographical regions for the respective operators and years.

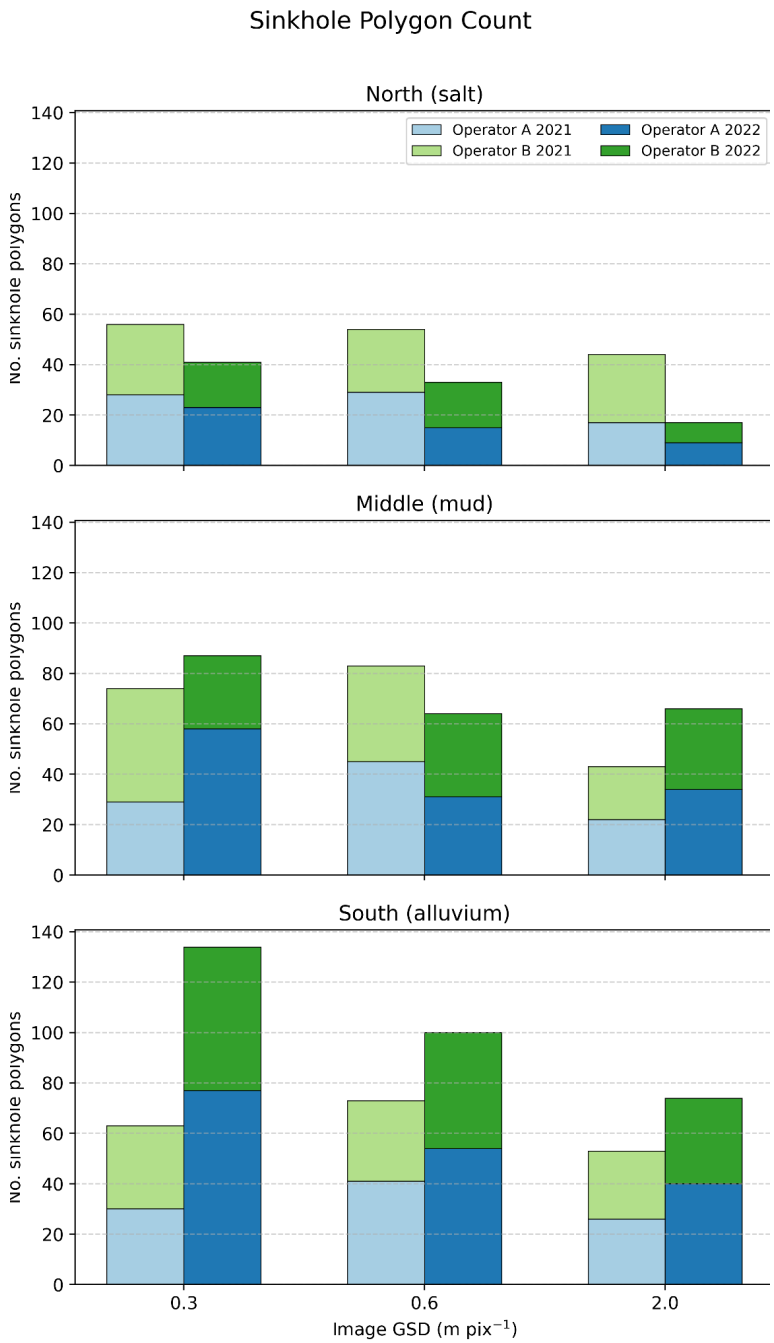


Figure S5: Polygon count by operator for the three sample areas for the 2021 and 2022 satellite images. The values in the table represent the number of sinkhole polygons observed at each specified GSD within the given geographical regions for the respective operators and years.

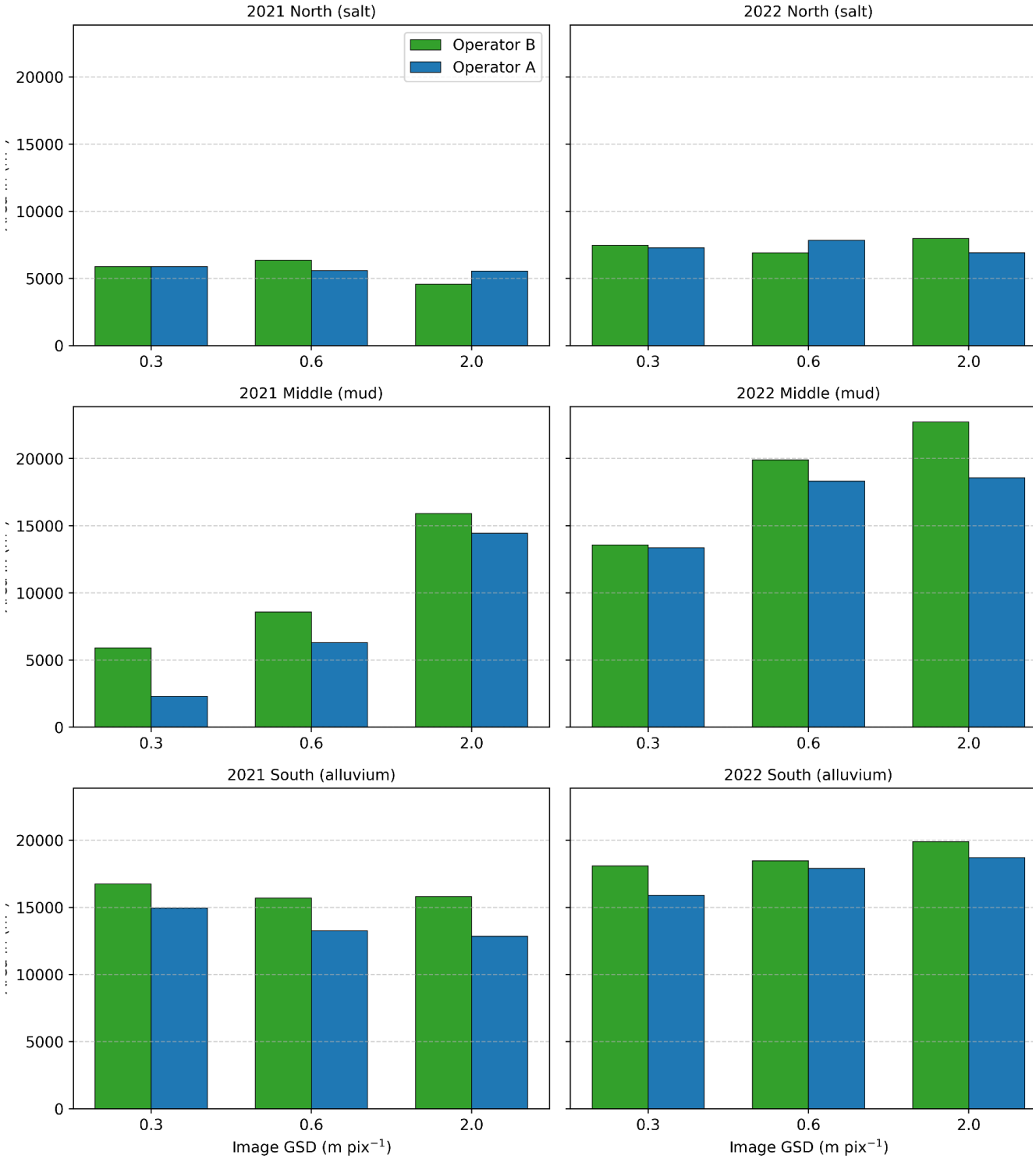


Figure S6: bar graph of the total sinkhole area mapped in different zones of Ghor Al-Haditha with different geological substrates (north is salt-dominated, middle is mud-dominated, and south is alluvium-dominated: see Fig. 11); for satellite imagery with different ground sample distances (GSDs) and operators. Differences due to the GSD, as well as the operator, are discernible.

Section S4: subsidence evolution at uvala U1

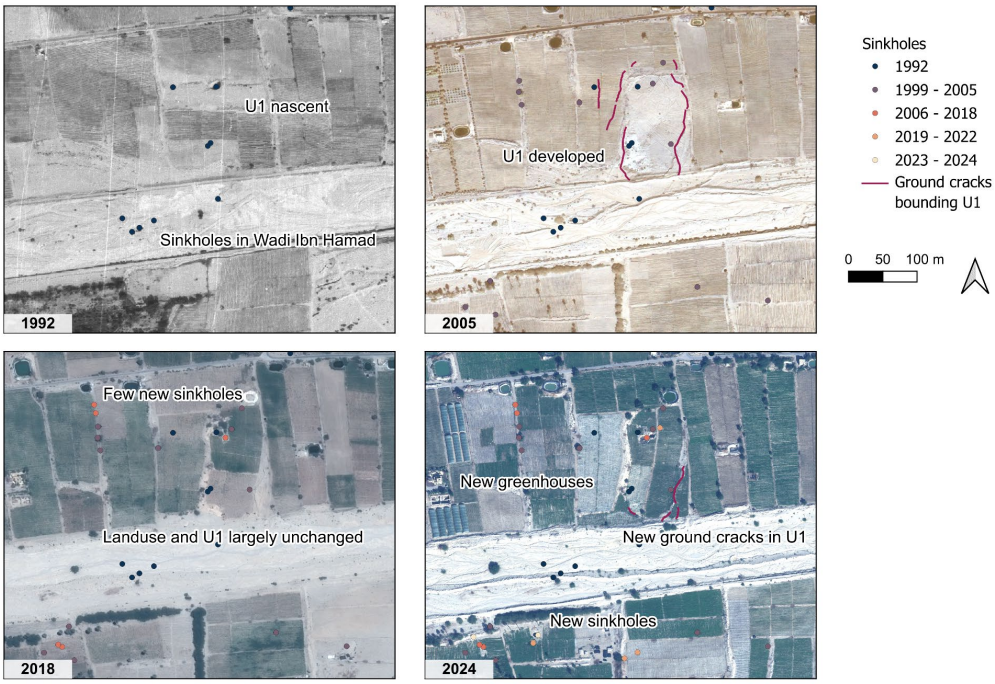


Figure S7: Resurgent development of sinkhole hazard during 2022-2023 in the south of Ghor Al-Haditha, close to uvala U1, which was thought to no longer be active since 2005. Base images are from (a) aerial survey of the Royal Jordanian Geographical Centre, (b) Quickbird satellite (© Maxar), (c) Pléiades 1A/B satellite (© CNES 2018, Distribution Airbus DS) and (d) Pléiades Neo satellite (© Airbus DS 2022).

Section S5: Supporting information for the sinkhole frequency distribution (scaling) analysis

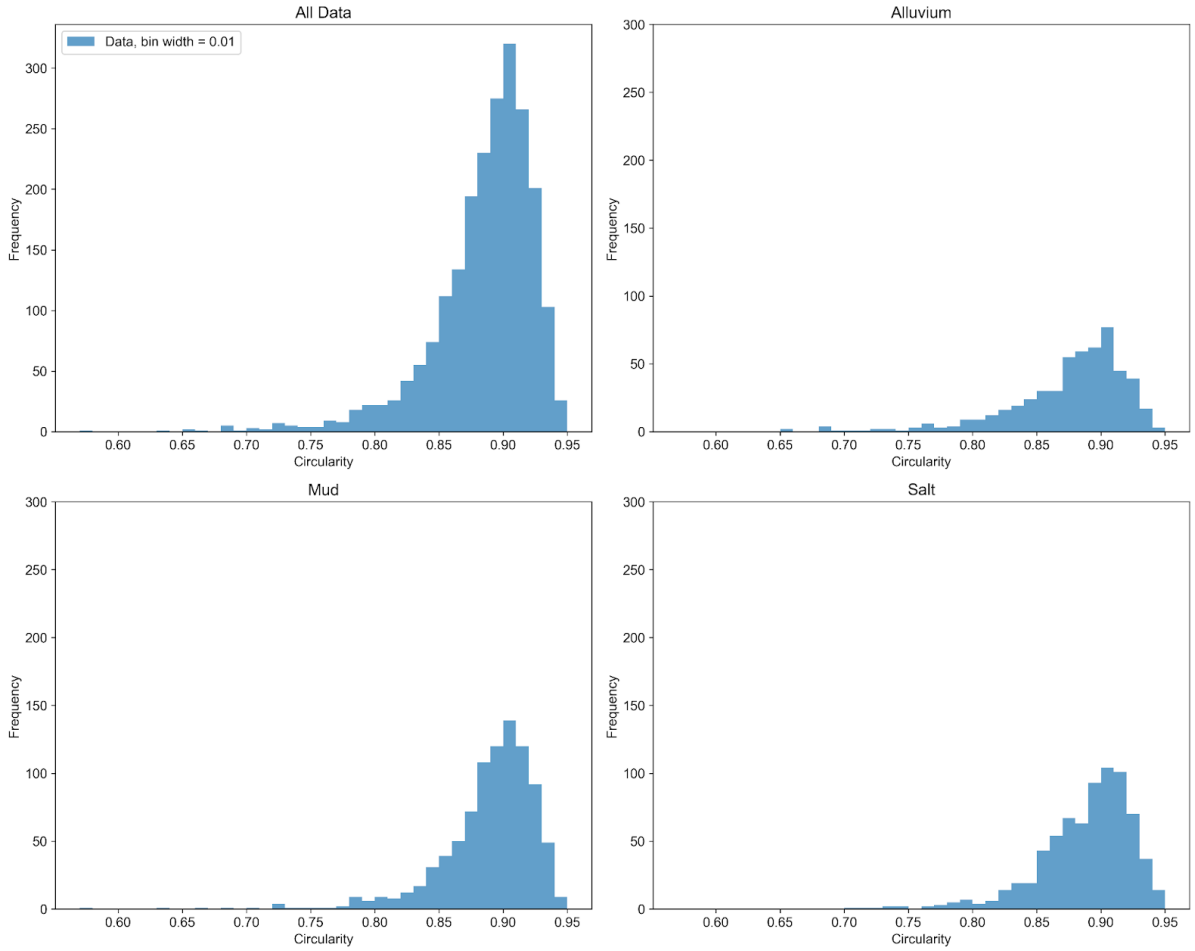


Figure S8: Circularity ratios for the sinkhole population. The ratio represents the relation between the area of the sinkhole and the area of a circle having a circumference equal to the perimeter of the sinkhole (equivalent area). A perfectly circular sinkhole has a circularity ratio of 1; as the irregularity of the sinkhole perimeter increases, the circularity ratio decreases.

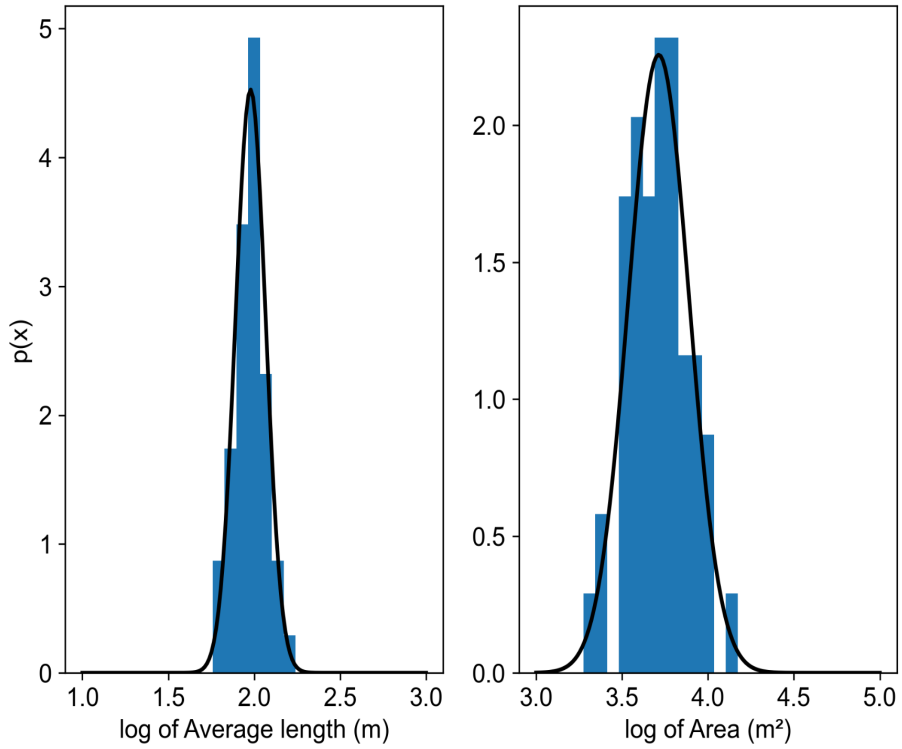


Figure S9: A first example of the distribution of the mean value of the log of 50 random subsets of sinkhole average length and area; n = 50 in both cases. For both length and area, the means of the log values are normally distributed, demonstrating that the data conform to the central limit theorem, though the visual fit for the area is not as good as for the average length.

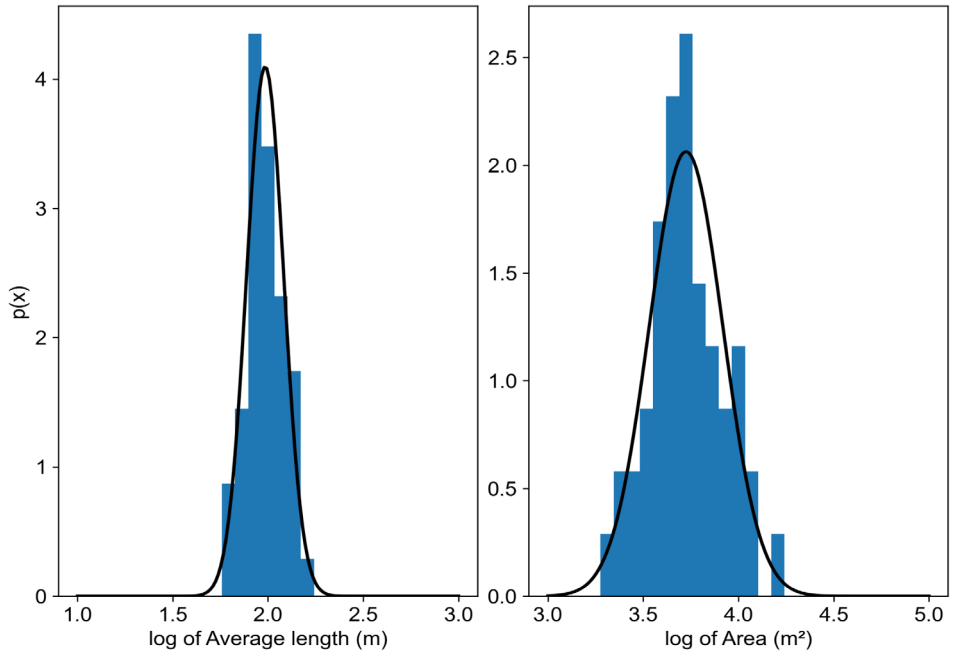


Figure S10: A second example of the distribution of the mean value of the log of 50 random subsets of sinkhole average length and area; n = 50 in both cases. For both length and area, the means of the log values are normally distributed, demonstrating that the data conform to the central limit theorem, though the visual fit for the area is not as good as for the average length.

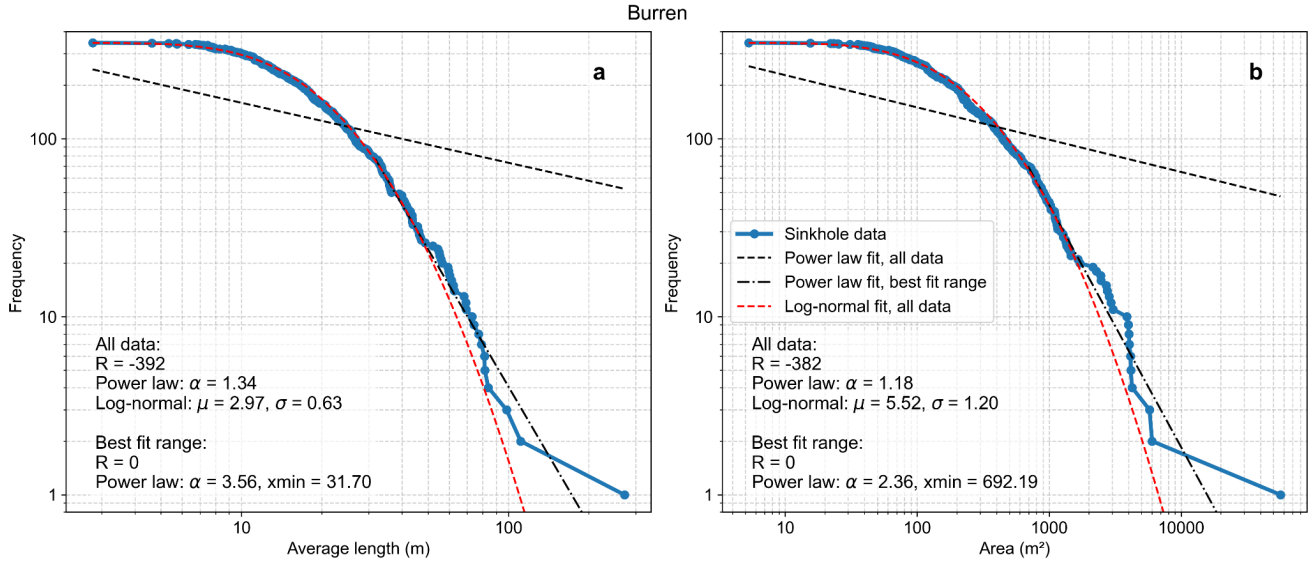


Figure S11: Cumulative frequency curves for (a) sinkhole average length and (b) sinkhole area for the Burren limestone karst in Ireland. In both cases, a power law fit can only be reasonably applied to the tail of the dataset (the larger sinkholes), whilst a lognormal fit reasonably approximates the entire distribution of sinkhole lengths and areas. The single largest sinkhole is a huge bedrock collapse sinkhole, Poll Berrin, which is something of an anomaly within the study area (cf. Watson et al., 2024).

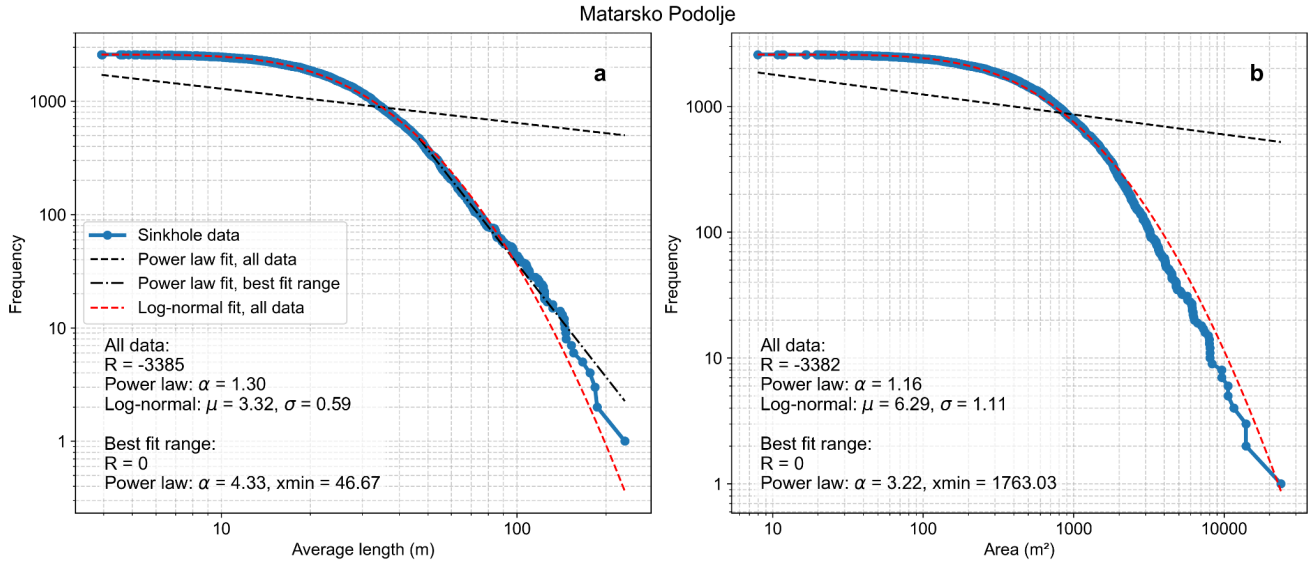


Figure S12: Cumulative frequency curves for (a) sinkhole average length and (b) sinkhole area for solution sinkholes from the Matarsko Podolje limestone karst area in Slovenia. In both cases, a power law fit can only be reasonably applied to the tail of the dataset (the larger sinkholes), whilst a lognormal fit reasonably approximates the entire distribution of sinkhole lengths and areas.

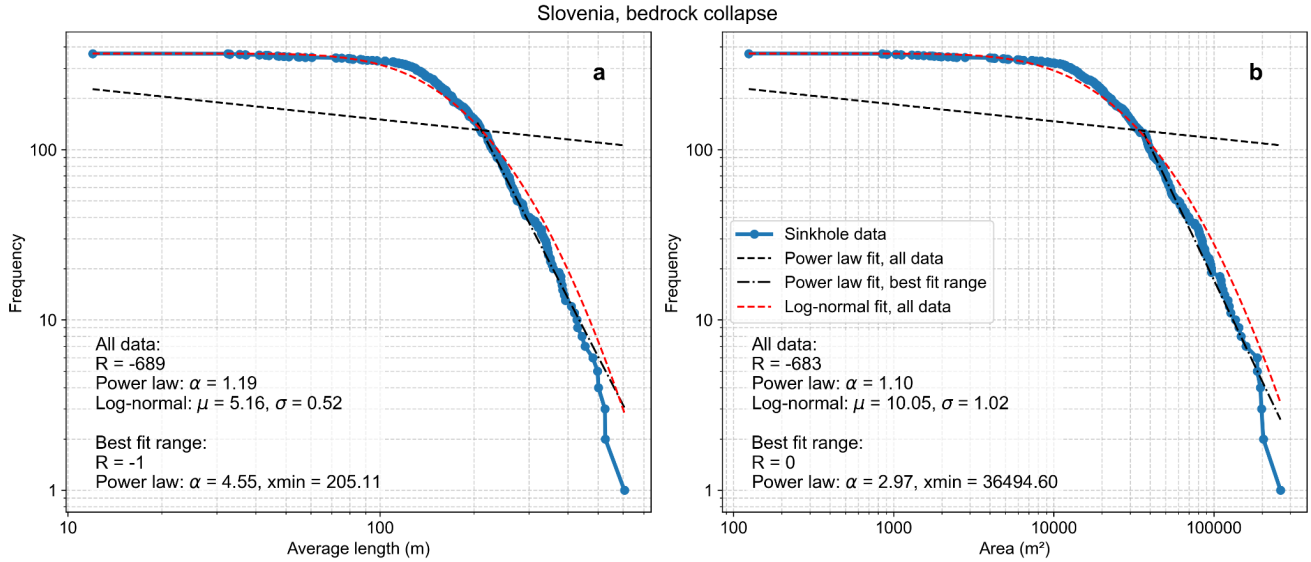


Figure S13: Cumulative frequency curves for (a) sinkhole average length and (b) sinkhole area for bedrock collapse sinkholes from karst areas across Slovenia. In both cases, a power law fit can only be reasonably applied to the tail of the dataset (the larger sinkholes), whilst a lognormal fit reasonably approximates the entire distribution of sinkhole lengths and areas.

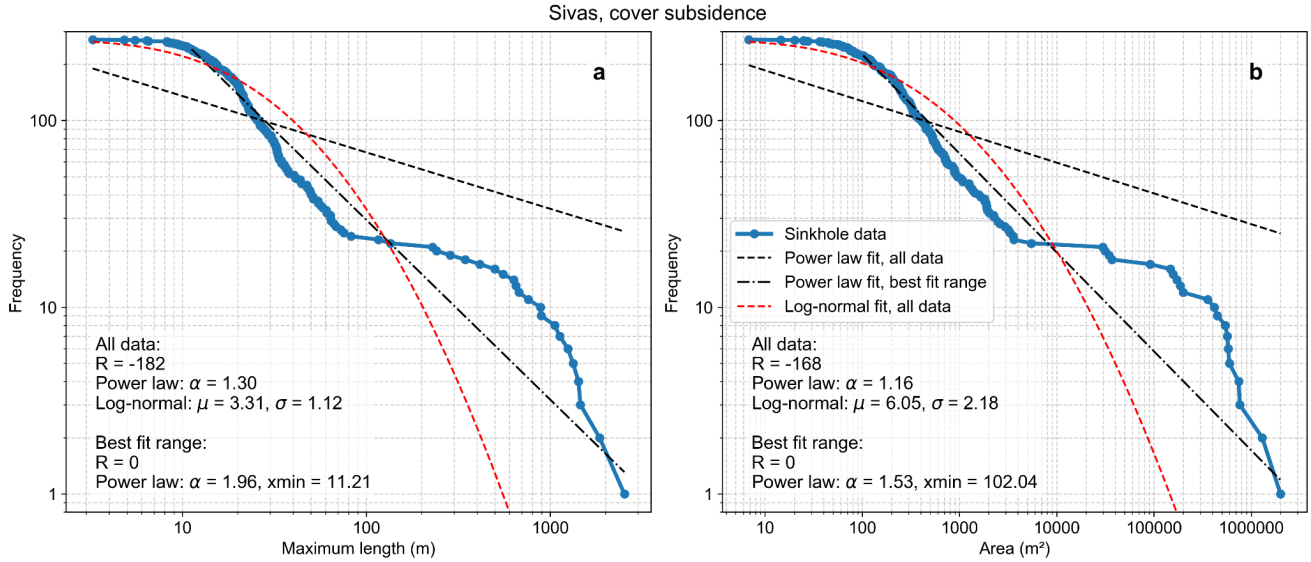


Figure S14: Cumulative frequency curves for (a) sinkhole average length and (b) sinkhole area for cover subsidence sinkholes from the Sivas gypsum karst in Turkiye.

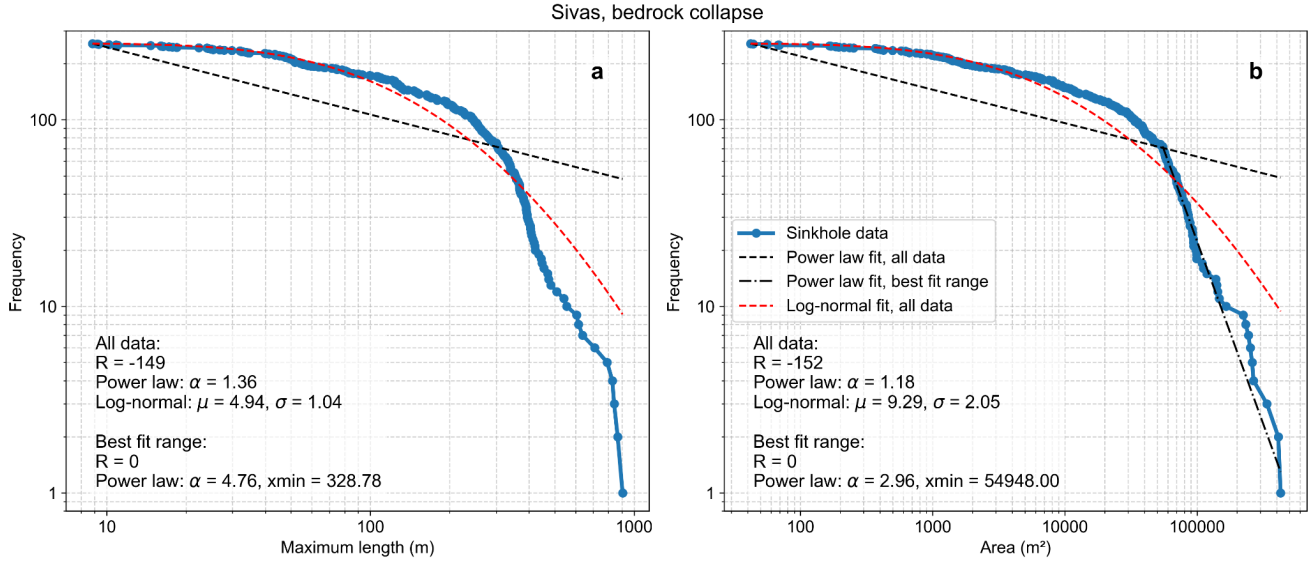


Figure S15: Cumulative frequency curves for (a) sinkhole average length and (b) sinkhole area for bedrock collapse sinkholes from the Sivas gypsum karst in Turkiye.